Communication

In Situ Observation and Growth Kinetics of Bainite Laths in the Coarse-Grained Heat-Affected Zone of 2.25Cr-1Mo Heat-Resistant Steel During Simulated Welding

YANG SHEN, BO CHEN, and CONG WANG

Austenite → bainite transformation has been documented *in situ* by confocal scanning laser microscope, and bainite growth kinetics has been quantified in the coarse-grained heat-affected zone of 2.25Cr-1Mo steel. Four typical nucleation sites of bainite laths have been identified. In addition, growth rate of nine distinctive bainite laths varies from 9 to 200 μm/s, depending on the degree of supercooling and nucleation sites of bainite laths.

https://doi.org/10.1007/s11661-020-06061-z

Low-alloy ferritic 2.25Cr-1Mo steel is extensively used as structural components in steam-generating systems of power plants.[1] Welding process is one of the key technologies for the application of such a heat-resistant steel grade. It is generally conceded that solid-state phase transformations in the coarse-grained heat-affected zone (CGHAZ) during welding processes profoundly influence the heterogeneous microstructure of welded joints, which to a large extent determines the final mechanical properties. Due to high peak temperature and rapid cooling rate in the CGHAZ,[2] austenite is quickly quenched to low temperature and could transform into ferrite, pearlite, bainite, or martensite.[3] Bainite, as the main CGHAZ microstructural constituent obtained from displacive austenite transformation in low-carbon low-alloy heat-resistant steel, is of practical importance in tuning excellent toughness and high strength. Consequently, adequate understanding of austenite → bainite phase transformation in the CGHAZ is essential to ensure the overall performance of the weldment.

Since Bain reported the first bainite in 1930s,[4] there has been a debate as to which mechanism dominates bainite transformation.[5–8] In previous studies, the morphology and transformation kinetics of bainite could only be examined in a post-mortem manner by conventional metallographic and modeling investigations. Lambert-Perlade *et al.*[9] investigated the morphological and crystallographic aspects of the austenite to bainite phase transformation in the CGHAZ of a low-alloy steel. Quidort *et al.*[10] proposed a kinetic model to describe both the nucleation and growth process for the overall transformation of austenite into bainite. However, most of the above results were based on *ex situ* observation.

Recently, Kang *et al.*[11] introduced *in situ* observation of bainite growth process by using a transmission electron microscopy with a hot stage during isothermal annealing. It was revealed that the shearing mechanism of bainite growth was controlled by the diffusion of solute atoms such as carbon. However, due to the fast heating and cooling rates of the actual welding process, the mechanisms of bainite growth obtained under isothermal conditions may not be applicable.

Fortunately, high-temperature confocal laser scanning microscopy (CSLM) emerges as a powerful *in situ* observation technique to investigate the kinetics of phase transformation and microstructural evolution in real time. Previous work has proven that it can provide sufficient topological contrast incurred by displacive phase transformation process, at larger temporal and dimensional scales.[12–15] Xu *et al.*[16] utilized CSLM for *in situ* observations of the morphological development of bainite transformation in a super bainite steel and found that bainite growth was characterized by the impingement of bainite sheaves, which resulted in an interlocking bainite microstructure. Furthermore, with the accessibility of electron backscatter diffraction (EBSD) technique, grain orientations and local strain distributions of the CGHAZ can be quantitatively analyzed, which enables better understanding of the microstructure development of bainite laths.[17, 18]

Therefore, the present work aims to characterize the continuous nucleation and growth process of bainite transformation and quantify the growth rate of individual bainite laths by *in situ* CSLM observation. Such information combined with the EBSD based *ex situ* crystallographic analysis enriches our understanding of the morphology and kinetics of bainite transformation in the CGHAZ of 2.25Cr-1Mo steel, and provides important insights about optimizing welding parameters and improving the performance of the weldment.

YANG SHEN is with the School of Metallurgy, Northeastern University, Shenyang 110819, P.R. China. BO CHEN is with the School of Engineering, University of Leicester, Leicester LE1 7RH, UK. CONG WANG is with the School of Metallurgy, Northeastern University and also with the State Key Laboratory of Rolling and Automation, Northeastern University, Shenyang 110819, P.R. China. Contact e-mail: wangc@smm.neu.edu.cn

Manuscript submitted August 31, 2020; accepted October 11, 2020. Article published online November 3, 2020

2.25Cr-1Mo steel plate (ASTM A378 Grade 22 Class 2) with 24 mm thickness is considered. It was normalized at 1203 K for 48 minutes and tempered at 1023 K for 84 minutes. The chemical composition of the steel is shown in Table I.

In situ observation of the nucleation and growth of bainite was carried out using a CSLM (VL2000DX-SVF18SP, Yonekura Manufacturing Corporation, Japan) with a purple laser diode (wavelength of 405 nm) and a halogen infrared heating lamp. A cylindrical specimen was prepared with the dimensions of 5 mm in diameter and 4 mm in height. The top and bottom surfaces of the specimen were ground, and the final polish employed a 0.25 μm suspension of diamond suitable for the CSLM observation. Then, the specimen was placed inside an alumina crucible, which was inserted into the furnace chamber on a Pt sample holder. A thermocouple was attached to the Pt sample holder to measure the temperature from the bottom of the crucible. The thermal cycle consisted of three steps: (1) heating to 473 K at a rate of 40 K/min, holding for 30 seconds, (2) heating to 1673 K ($T_p \gg Ac_3$ = 1117 K) at 1000 K/min, holding for 20 seconds, and (3) continuously cooling to room temperature at programmed cooling rate, as shown in Figure 1. This thermal cycle was designed especially for simulating the thermal cycle of CGHAZ adjacent to the weld fusion line in shielded metal arc welding (SMAW) process with 18 kJ/cm heat input. During the experiment, the furnace was filled with high-purity argon to prevent oxidation, and successive images were recorded at a rate of 15 frames per second and were collected by a charge-couple device (CCD) camera.

After *in situ* observation, crystallographic information was analyzed by a field-emission scanning electron microscope (FESEM, MAIA3 XMH, TESCAN, CZ) operating at 20.0 kV, which is coupled with an EBSD system (NordlysMax^3, Oxford Instruments) and HKL CHANNEL5 software. A step size of 0.1 μm was used. More detailed descriptions for EBSD specimen preparation are presented elsewhere.[19, 20]

Figure 2 shows typical CSLM snapshots of austenite to bainite phase transformation observed *in situ* under the cooling cycle of a simulated CGHAZ. It is noteworthy that the images in CSLM are attained by displacive motion as a result of surface relief.[21, 22] As shown by the red circle in Figure 2(a), bainite phase transformation occurs at 687 K according to the apparent surface relief. It is observed that numerous parallel bainite laths (B_1) first nucleate on the grain boundary of austenite and grow in a straight line into the grain at an angle of 40 deg inclined to the grain boundary, as highlighted by red dotted square in the inset of Figure 2(a). Simultaneous and continuous nucleation of bainite sheaves occurring on the grain boundary implies that in cases where bainite laths have not been previously formed, the boundary of the austenite grain is the preferred site for nucleation. This finding is consistent with the results that had been revealed by Mao *et al.*[23] After a short growth, the second bainite lath (B_2) nucleates at the tip of existing bainite laths (B_1) and grows rapidly with an inclined angle of 30 deg to B_1, as shown by the green circles in Figures 2(b) and (c). Concurrently, it can be seen that another newly formed bainite lath (B_3) is also attached to the previous laths (B_1) and grows in the same direction as B_2, as shown by the blue circles in Figures 2(c) and (d). These features indicate that the tip of the existing bainite laths is the favorable site for the nucleation of the later bainite laths.

With the increase of cooling time, as displayed by the magenta circles in Figures 2(d) through (g), the fourth bainite lath (B_4) nucleates on the other side of the austenite grain boundary and grow in a direction of 30 deg inclined to it. Upon further cooling, as shown by the yellow and cyan dotted squares in the inset of Figures 2(e) and (f), respectively, the fifth (B_5) and sixth (B_6) bainite laths start to nucleate on an inclusion at 676 K and grow in opposite directions. Subsequently, the seventh bainite lath (B_7) nucleates on grain boundary again and grows in parallel to B_4, which is represented by the violet circles in Figures 2(g) and (h). The last nucleation site of bainite laths is grain interior, as shown by the dark red and black dotted squares in the inset of Figure 2(h), where the eighth (B_8) and the ninth (B_9) bainite laths start to nucleate inside the grain at 668 K and then extend at a high rate in the interior of austenite grain. As phase transformation

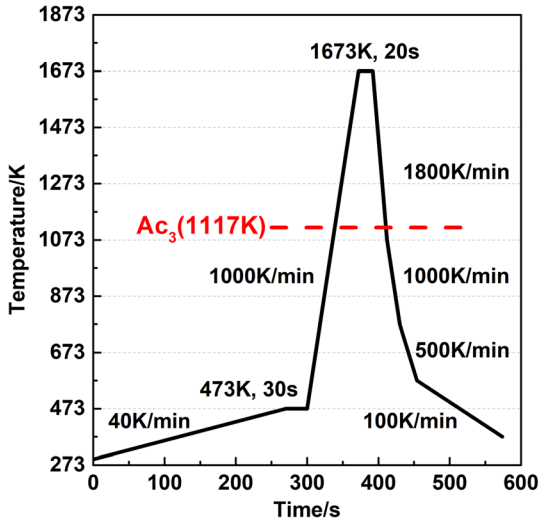

Fig. 1—Thermal cycle employed for *in situ* observation under CSLM.

Table I. Chemical Composition of 2.25Cr-1Mo Steel (Weight Percent)

C	Mn	P	S	Si	Cr	Mo	Ni
0.141	0.557	0.0049	0.0015	0.092	2.395	0.967	0.157

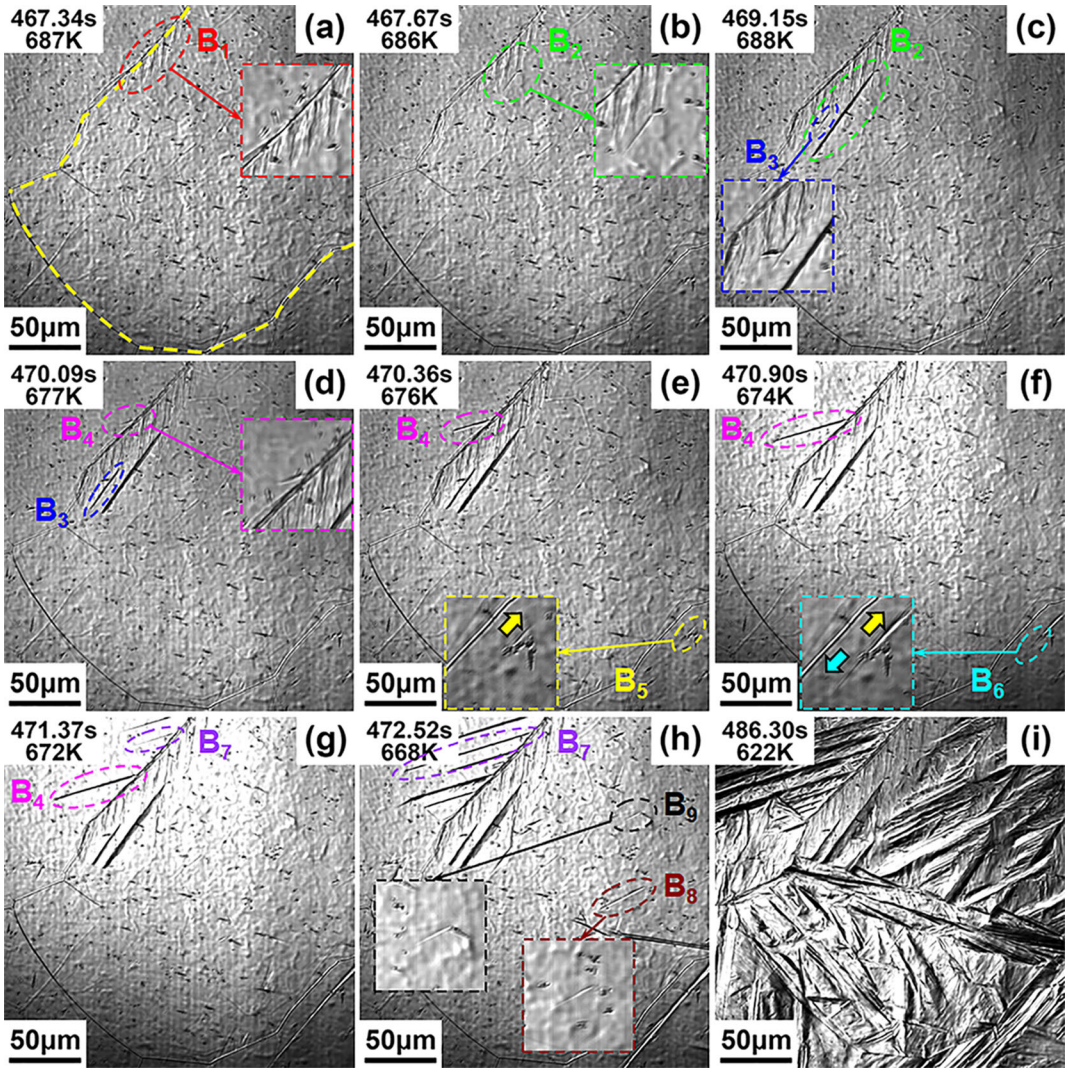

Fig. 2—(*a*) through (*i*) CSLM snapshots tracking continuous nucleation and growth of bainite laths. (Austenite grain boundaries are indicated by yellow dash lines; B_1, B_2, B_3, B_4, B_5, B_6, B_7, B_8, and B_9 with different colors represent the growing bainite laths) (Color figure online).

progresses, subsequent bainite laths are always attached to the preceding laths by its side and grow parallel to them, leading to the formation of wider bainite sheaves. As shown in Figure 2(i), bainite laths cover the entire prior austenite grain at 622 K and exhibit a typical feathery upper bainite morphology based on the last registered CSLM observation.

It is well known that bainitic transformation preferentially nucleates at those locations where the energy barrier is low. The energy barriers for different bainite nucleation sites are different. Risks *et al.*[24] and Xu *et al.*[25] ranked all possible nucleation sites in the increasing order of difficulty from phase boundaries, grain boundaries, stacking fault, inclusions, to free surface. Therefore, in the present study, bainite laths are expected to preferentially nucleate on grain boundaries rather than on the surface of inclusions or austenite matrix, which are consistent with previous studies.[26]

Quantitative results of respective growth rate of the above nine bainite laths are shown in Figure 3, which were measured from successive CSLM images using the Image J software. Figure 3(a) shows three typical growth rates of bainite laths nucleated on grain boundaries. The growth rate of B_1 (9 to 15 μm/s) varies within a certain range due to simultaneous nucleation of numerous parallel bainite laths. Furthermore, it is observed that growth rates of B_4 (61 μm/s) and B_7 (99 μm/s) sharply increase with decreasing temperature. As shown in Figure 3(b), B_2 and B_3, which nucleate at the tip of the existing lath (B_1), extend very fast at a rate of 141 and 107 μm/s, respectively. The lengthening rate of the newly formed single bainite laths (B_2 and B_3) is faster than that of the bainite sheaf (B_1) because of the inhibition effects between successive growth of bainite platelets.[27] Figure 3(c) presents a distinct contrast in the growth rate of the two bainite laths nucleated on the same inclusion. The growth rate of bainite lath (B_5) is 34 μm/s. However, the other bainite lath (B_6), which subsequently grows in the opposite direction to B_5, extends very quickly at a rate of 207 μm/s. The reason for the appreciable change in growth rate could be explained by the idea that high strain energy around the inclusion arising from displacive motion of bainite laths may render the nucleation and growth of the

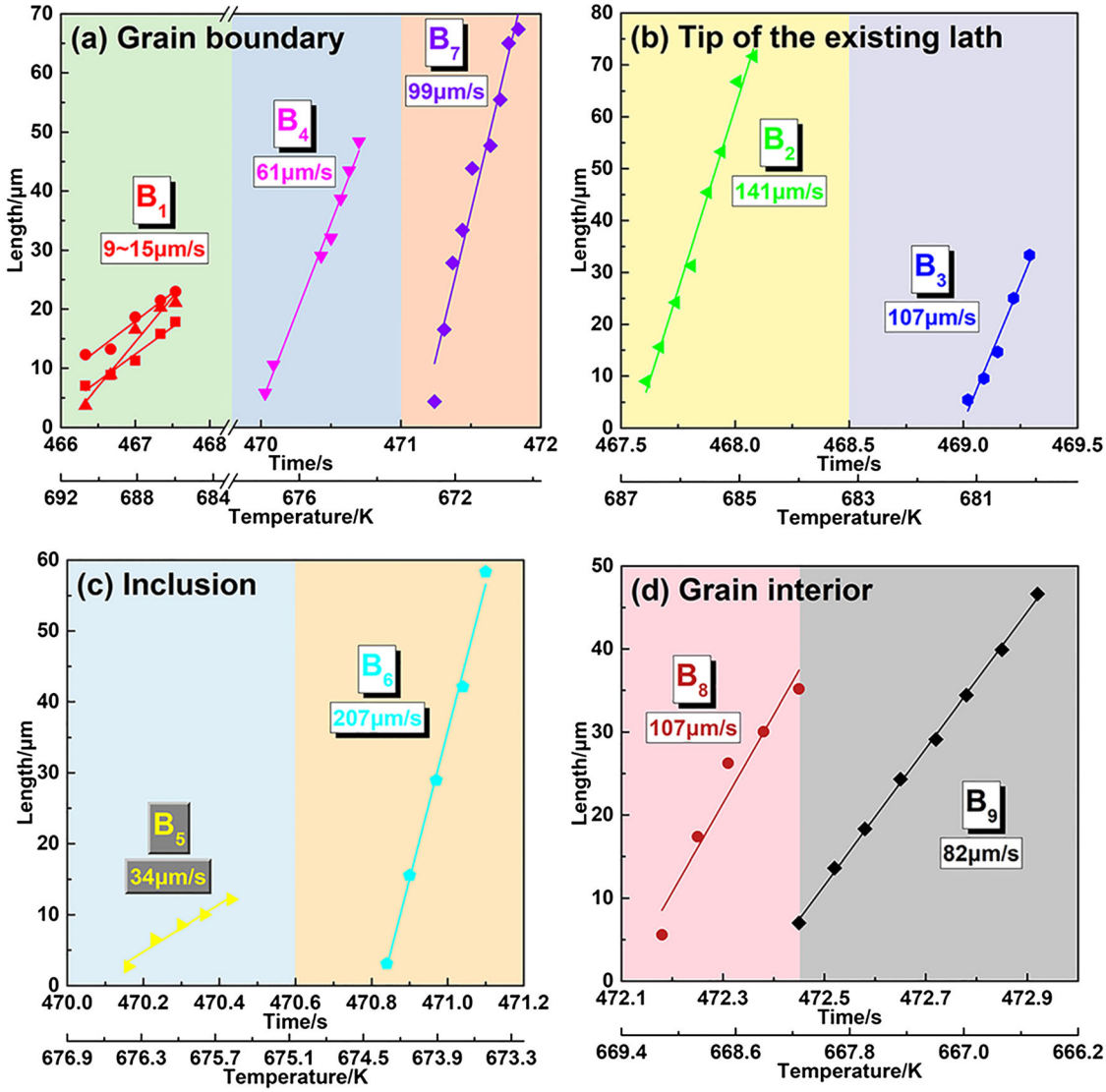

Fig. 3—Plots of growing bainite length against cooling time for four typical nucleation sites: (*a*) grain boundary, (*b*) tip of the existing lath, (*c*) inclusion, and (*d*) grain interior.

subsequent bainite laths relatively easy.[28] As shown in Figure 3(d), although B_8 and B_9 nucleate relatively late inside the grain, they cover the entire austenite grains at a faster speed of 107 and 82 μm/s, respectively.

In order to facilitate the understanding of the effect of temperature gradient on the growth rate of bainite lath during the cooling process, it is assumed that the temperature (687 K) at which bainite lath first appears is the theoretical bainite transformation temperature. Therefore, with the decrease of temperature, the degree of supercooling (ΔT) of B_1, B_4, B_7, and B_8 is $\Delta T_1 = 0$ K, $\Delta T_4 = 10$ K, $\Delta T_7 = 15$ K, and $\Delta T_8 = 18$ K, respectively. In addition, the diffusivity of carbon in austenite (D) as a function of temperature follows an Arrhenius law[29, 30]:

$$D = D0 \exp\left(-\frac{Q}{\mathrm{RT}}\right), \qquad [1]$$

where D_0 is a constant with its value given as 2.0×10^{-5} m^2/s in Reference 31, Q is activation energy, and R is gas constant. According to Eq. [1], with the decrease of temperature, the value of D will decrease to $D_1 = 4.5 \times 10^{-16}$ m^2/s, $D_4 = 3.2 \times 10^{-16}$ m^2/s, $D_7 = 2.6 \times 10^{-16}$ m^2/s, and $D_8 = 2.3 \times 10^{-16}$ m^2/s, for bainite lath of B_1, B_4, B_7, and B_8, respectively.

Generally, it is considered that bainite transformation includes two stages of nucleation and growth, which are simultaneously affected by ΔT and D. The nucleation of bainite nuclei is mainly controlled by carbon diffusion due to the relatively large D and small ΔT, whereas the growth of bainite laths is dominated by the shearing mechanism.[32]

As the temperature decreases, ΔT will be enhanced, which will most likely promote bainite growth kinetics. Endo *et al.*[33] investigated a relationship between ΔT and growth rate in $Y_1Ba_2Cu_3O_{7-x}$ superconductor and found that the growth rate exhibited an increasing trend with increasing ΔT ($\Delta T < 20$ K), following the parabolic pattern. Moreover, it is generally accepted that the higher cooling rate is, the lower actual phase

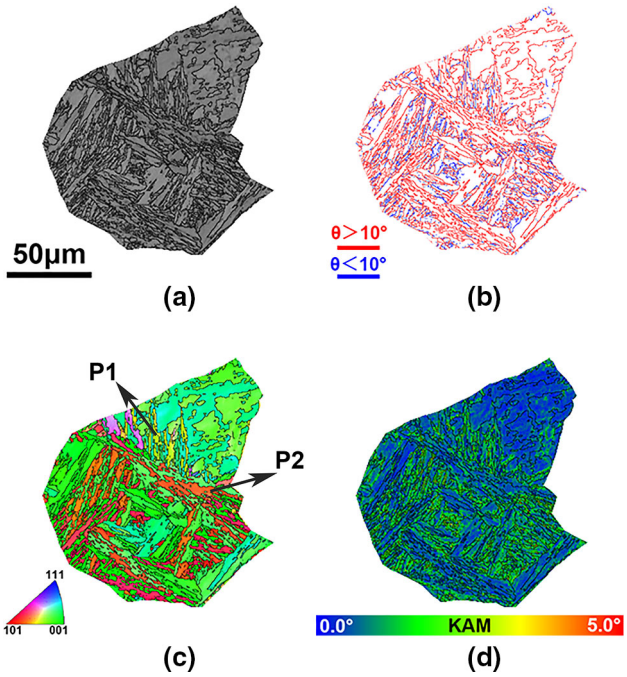

Fig. 4—Crystallographic characteristics of CGHAZ analyzed by EBSD: (*a*) band contrast map, (*b*) grain boundary map, (*c*) inverse pole figure, and (*d*) kernel average misorientation map. (P1 and P2 represent two packets of lath bainite in a prior austenite grain).

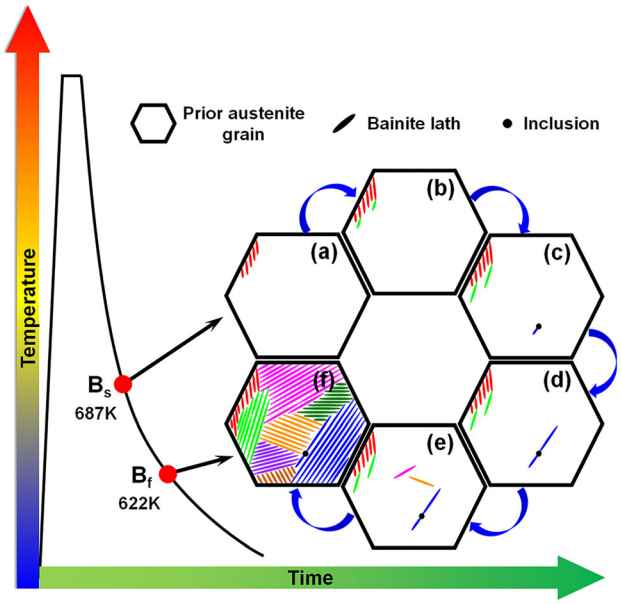

Fig. 5—Schematic illustration of the bainite transformation of steel subjected to simulated welding thermal cycle: (*a*) nucleation on grain boundary, (*b*) nucleation on tip of the existing bainite lath, (*c*) nucleation on inclusion, (*d*) nucleation on inclusion and grow in the opposite direction, (*e*) nucleation on grain interior, and (*f*) growth of bainite lath.

transformation temperature is, leading to the higher ΔT.[34] Mao *et al.*[23] analyzed the influence of different cooling rates (0.2, 1, and 5 K/s) on the growth rate of bainite laths in low-carbon bainite weld metal. They discovered that the actual bainite transformation temperature for each cooling rate was 698.4 K, 677.3 K, and 636.2 K, respectively, and the corresponding average growth rate was 2.25 μm/s (0.2 K/s), 183 μm/s (1 K/s), and 1979 μm/s (5 K/s), respectively. By assuming that the theoretical bainite transformation temperature is constant, the cooling rate difference between 0.2 and 1 K/s would result in a ΔT value difference of 21.1 K, whereas 41.1 K for the cooling rate between 0.2 and 5 K/s. The above-mentioned results seem to suggest that the growth rate of bainite lath is highly sensitive to the cooling rate due to the degree of supercooling ΔT.

In the present work, the growth rate of B_8 is about 10 times faster than that of B_1 ($\Delta_{1-8} = 18$ K). The variation trend of growth rate of bainite laths caused by ΔT is broadly consistent with previous studies, but the quantitative relationship between ΔT and the growth rate remains ambiguous. Therefore, a plausible explanation for the vast growth-rate difference for the four bainite laths (B_1, B_4, B_7, and B_8) is most likely to be dominated by the degree of supercooling ΔT. In addition, comparing the growth rates of the nine bainite laths upon four characteristic nucleation sites, the variation in growth rates, from 9 μm/s to higher than 200 μm/s, could also be enabled by the difference of nucleation sites of bainite laths, which may likely be associated with irregular atomic arrangements, lattice distortions, and defects.[27,28,35]

Detailed crystallographic features of the CGHAZ after simulated welding cycle by EBSD are presented in Figure 4. The band contrast map in Figure 4(a) shows a typical bainitic microstructure within a single large prior austenite grain (PAG). Figure 4(b) depicts the multiple boundary structure distribution based on the misorientation of adjacent points of the EBSD data, and misorientation boundaries of 2 to 10 deg and over 10 deg are defined as low angle grain boundaries (LAGBs) and high-angle grain boundaries (HAGBs). It can be observed that the dominant grain boundaries are HAGBs with red lines, and only a negligible part of lath bainitic boundaries are LAGBs denoted by blue lines. Normalized frequency of HAGBs is 80.9 pct, while that of LAGBs is 19.1 pct. It has been well known that HAGBs can effectively arrest the propagation of cleavage microcracks and improve toughness.[9,36] Therefore, it can be inferred that CGHAZ may show excellent toughness due to the high frequency of HAGBs in a single austenite grain. As clearly displayed in the inverse pole figure in Figure 4(c), PAG is divided into numerous bainitic packets (such as P1 and P2) as indicated by the black arrows, which grow in different directions with HAGBs. In addition, the crystallographic orientation of some bainite laths is virtually the same even if they are separated by a good distance, which may belong to the same variant pairs in Kurdjumov–Sachs (K-S) orientation relationship.[37] Kernel average misorientation (KAM) map in Figure 4(d) shows the high local strain levels or crystal deformations of the grains, which indicate the high degree of the bainitic transformation in the CGHAZ.

Based on the observation and discussion above, a typical schematic illustration of the bainite nucleation and growth process is depicted in Figure 5. As shown in Figures 5(a) through (f), it suggests that numerous parallel bainite laths tend to nucleate on the grain boundary where few bainite laths previously formed. However, once bainite laths have nucleated on the boundary, subsequent bainite laths will nucleate at the tip of the existing bainite laths immediately, and grow at an angle inclined to the existing lath. Moreover, inclusion and grain interior are another two important locations for the nucleation and growth of bainite laths. During continuous cooling of the welding process, the growth rate of bainite lath sharply increases with decreasing temperature, which could be attributed to the degree of supercooling.

In summary, the present study illustrates a combined *in situ* observation with post-mortem EBSD characterization study of microstructure evolution and bainite transformation kinetics in the CGHAZ of 2.25Cr-1Mo steel under simulated welding condition. Main conclusions are as follows:

1. *In situ* CSLM observations suggest that four characteristic nucleation sites of bainite laths in the CGHAZ are put forward, which are considered to be on grain boundaries, tips of the existing laths, inclusions, and grain interior, respectively.
2. A number of bainite laths in four typical nucleation sites are systematically analyzed, and it is elucidated that bainite lath growth rates varies at a wide range from 9 μm/s to higher than 200 μm/s, which is largely affected by the degree of supercooling.

The authors wish to thank the financial supports from the National Natural Science Foundation of China (51861130361, 51850410522, 51861145312, and 52011530180), Newton Advanced Fellowship by the Royal Society (RP12G0414), The Fundamental Research Fund for Central Universities (N172502004, N182506002, and N2025025), Natural Science Foundation of Liaoning (2019KF0502), and Xingliao Talents Program (XLYC1807024 and XLYC1802024). The authors also greatly appreciate the support from Dr. Tongsheng Zhang from Central South University. Bo Chen acknowledges financial supports by the UK's Engineering and Physical Sciences Research Council, EPSRC Early Career Fellowship Scheme EP/R043973/1.

REFERENCES

1. K. Laha, K.S. Chandravathi, K. Bhanu Sankara Rao, S.L. Mannan, and D.H. Sastry: *Metall. Mater. Trans. A*, 2001, vol. 32A, pp. 115–24.
2. Y. Li and T.N. Baker: *Mater. Sci. Technol.*, 2010, vol. 26, pp. 1029–40.
3. E. Schmidt, Y. Wang, and S. Sridhar: *Metall. Mater. Trans. A*, 2006, vol. 37A, pp. 1799–810.
4. E.S. Davenport and E.C. Bain: *Metall. Trans.*, 1970, vol. 1, pp. 3503–30.
5. R.F. Hehemann, K.R. Kinsman, and H.I. Aaronson: *Metall. Trans. A*, 1972, vol. 3, pp. 1077–94.
6. H.K.D.H. Bhadeshia: *Mater. Sci. Eng. A*, 1999, vol. 273, pp. 58–66.
7. H.I. Aaronson, W.T. Reynolds, G.J. Shiflet, and G. Spanos: *Metall. Trans. A*, 1990, vol. 21, pp. 1343–80.
8. M. Hillert: *ISIJ Int.*, 1995, vol. 35, pp. 1134–40.
9. A. Lambert-Perlade, A.F. Gourgues, and A. Pineau: *Acta Mater.*, 2004, vol. 52, pp. 2337–48.
10. D. Quidort and Y.J.M. Brechet: *ISIJ Int.*, 2002, vol. 42, pp. 1010–17.
11. M. Kang, M.-X. Zhang, and M. Zhu: *Acta Mater.*, 2006, vol. 54, pp. 2121–29.
12. X. Zou, J. Sun, H. Matsuura, and C. Wang: *Metall. Mater. Trans. B*, 2018, vol. 49B, pp. 2168–73.
13. W. Mu, P. Hedström, H. Shibata, P.G. Jönsson, and K. Nakajima: *JOM*, 2018, vol. 70, pp. 2283–95.
14. X. Yu, S.S. Babu, J.C. Lippold, H. Terasaki, and Y.I. Komizo: *Metall. Mater. Trans. A*, 2012, vol. 43A, pp. 1538–46.
15. Y. Shen, B. Chen, and C. Wang: *Metall. Mater. Trans. A*, 2020, vol. 51A, pp. 3371–76.
16. G. Xu, F. Liu, L. Wang, and H. Hu: *Scripta Mater.*, 2013, vol. 68, pp. 833–36.
17. F.J. Humphreys: *J. Mater. Sci.*, 2001, vol. 36, pp. 3833–54.
18. S.I. Wright, M.M. Nowell, and D.P. Field: *Microsc. Microanal.*, 2011, vol. 17, pp. 316–29.
19. Y. Shen and C. Wang: *Metall. Mater. Trans. B*, 2019, vol. 50B, pp. 595–600.
20. Y. Shen, J. Leng, and C. Wang: *J. Mater. Sci. Technol.*, 2019, vol. 35, pp. 1747–52.
21. H. Terasaki and Y.I. Komizo: *Scripta Mater.*, 2011, vol. 64, pp. 29–32.
22. T. Ko and S.A. Cottrell: *J. Iron Steel Inst.*, 1952, vol. 172, pp. 307–12.
23. G. Mao, R. Cao, X. Guo, Y. Jiang, and J. Chen: *Metall. Mater. Trans. A*, 2017, vol. 48A, pp. 5783–98.
24. R. Ricks, P. Howell, and G. Barritte: *J. Mater. Sci.*, 1982, vol. 17, pp. 732–40.
25. Z. Xu, X. Jin, and J. Zhang: *Phase Tansformation in Materials*, 1st ed., Higher Education Press, Beijing, 2013, pp. 87–99.
26. H. Terasaki and Y.-I. Komizo: *Metall. Mater. Trans. A*, 2013, vol. 44A, pp. 2683–89.
27. H.K.D.H. Bhadeshia and D.V. Edmonds: *Metall. Trans. A*, 1979, vol. 10, pp. 895–907.
28. S. Zhang, N. Hattori, M. Enomoto, and T. Tarui: *ISIJ Int.*, 1996, vol. 36, pp. 1301–09.
29. C. Wells, W. Batz, and R.F. Mehl: *JOM*, 1950, vol. 2, pp. 553–60.
30. P. Thibaux, A. Métenier, and C. Xhoffer: *Metall. Mater. Trans. A*, 2007, vol. 38A, pp. 1169–76.
31. E.A. Brandes and G.B. Brook: *Smithells Metals Reference Book*, 7th ed., Elsevier, Oxford, 1992, pp. 994–95.
32. M. Zhou, G. Xu, L. Wang, and H. Hu: *Trans. Indian Inst. Met.*, 2016, vol. 69, pp. 693–98.
33. A. Endo, H.S. Chauhan, Y. Nakamura, and Y. Shiohara: *J. Mater. Res.*, 1996, vol. 11, pp. 1114–19.
34. G. Liang, Y. Ali, G. You, and M.-X. Zhang: *Materialia*, 2018, vol. 3, pp. 113–21.
35. Z.W. Hu, G. Xu, H.J. Hu, L. Wang, and Z.L. Xue: *Int. J. Miner. Metall. Mater.*, 2014, vol. 21, pp. 371–78.
36. X. Li, X. Ma, S.V. Subramanian, R.D.K. Misra, and C. Shang: *Metall. Mater. Trans. E*, 2015, vol. 2E, pp. 1–11.
37. H. Terasaki and Y.-I. Komizo: *Metall. Mater. Trans. A*, 2013, vol. 44A, pp. 5289–93.